Chapter 4

# Structural Modifications of KrF Excimer Laser-Ablated Zirconium Correlated to the Surface and Mechanical Properties

Nisar Ali, Umm-i-Kalsoom, Shazia Bashir and Narjis Begum

Additional information is available at the end of the chapter

http://dx.doi.org/10.5772/intechopen.70952

**Abstract**

The structural modifications of KrF excimer laser-ablated zirconium (Zr) have been investigated in correlation with its surface and mechanical properties after ablation in deionized water and ethanol. KrF excimer laser of pulse duration of 20 ns, wavelength of 248 nm, and repetition rate of 20 Hz has been utilized for this purpose. Irradiation of Zr was carried out for varying number of laser pulses ranging from 500 to 2000 for laser fluence value of 3.6 J/cm$^2$. The structural and chemical analyses were performed by using X-ray diffraction (XRD), Raman spectroscopy, and energy dispersive X-ray spectroscopy (EDS) techniques. Scanning electron microscope (SEM) and Vickers hardness tester were utilized for the analysis of surface morphology and hardness of laser-irradiated Zr targets. Presence of surrounding liquids played substantial role in structural, chemical, and mechanical modifications of Zr targets after irradiation. Pressure gradients and convective bubble motion owing to the confinement effects of the surrounding liquids, several thermal and chemical phenomena produced by heating through laser at the solid-liquid interface results in the generation of various hydrides and oxides of Zr, which are responsible for the development of various surface features and increase in hardness of irradiated Zr.

**Keywords:** zirconium, laser ablation, ambient environment, crystallinity, surface morphology, hardness

## 1. Introduction

Laser-induced micro and nanostructuring of materials is a versatile approach to modify the material properties for enhanced thermal properties [1], optical absorption [2], field emission

properties [3], biocompatibility [4], hydrophobicity [5], and tribological performance [6]. The interaction of laser radiations with solid materials, accompanied by a variety of instabilities, may result in the formation of various surface features, for example, laser-induced periodic surface structures (LIPSSs), cracks, nanodots, nanopores or nanocavities, and grains [7, 8].

Nanofabrication based on laser ablation strongly depends on parameters of laser beam, such as number of pulses, pulse duration, wavelength, fluence, and material's nature as well as the environmental conditions and their nanochemical effects [8]. With increasing number of pulses, the incubation effects become dominant, causing the reduction in ablation threshold of the irradiated material. For metallic targets, incubation effects are related to the accumulation of plastic deformation produced by laser-induced thermal stresses [9]. Materials ablation in liquid-confined environment has become an important technique for the production of debris-free microstructures on material's surface. The presence of a dense medium adjoining to the molten layer of the target causes various instabilities. Various kinds of structures can be grown due to the viscous flow of the vapors of the surrounding liquid and its chemical reaction with the metals. Shock wave generation, confinement and shielding effects, different cooling and quenching rates, and different chemical reactivity of the environment significantly affects the ablation efficiency of the target material [1, 8] without momentous effect on the stoichiometry of the target, and results in the development of cavitation bubbles and colloids owing to the formation of metal alcohols and oxides. Several physical processes such as formation of plasma, condensation, agglomeration, nucleation and coalescence are accountable for the formation and growth of nanostructures in the presence of reactive environment [10]. Particles and nanostructures produced by this process show liquid's dense vapors interaction with the molten layer produced on the surface of target. Such interactions are attributable to hydrodynamic instabilities under such circumstances. The molten layer acts as a source for the formation of nanoparticles and nanostructure. When beam focus passes through liquids, several nonlinear effects [11] as well as higher harmonic generation, filamentation and self-phase modulation take place. Considerable literature is already reported on liquid-based pulsed laser ablation of metals. Barminaa et al. reported the improvement in thermionic properties of tungsten surface after ablation in liquid environment [12]. Ablation of materials in the presence of surrounding liquid includes heat transfer through convection/conduction and motion of bubbles, which is responsible for the removal of particles redeposited over the surface and reduces the oxidation of debris [13]; as a result, the enhanced coupling of energy to the target is directed to hygienic and clean target surface [14].

The purpose of structural, surface, and mechanical modification of Zr by irradiation with nanosecond laser is to develop and alter its widespread functional, physical, chemical, and mechanical characteristics such as wear, hardness, and corrosion resistance etc. The development of several surface structures can be well associated with the increase of chemical reactivity of Zr. To achieve the enhanced chemical and mechanical properties, Zr targets were irradiated with KrF excimer laser for varying number of pulses ranging from 500 to 2000, in the presence of deionized water and ethanol. Various diagnostic techniques such as X-ray diffractometry (XRD), energy dispersive X-ray spectroscopy (EDS), Raman spectroscopy, scanning electron microscope (SEM), and Vickers hardness techniques were utilized to relate the

http://dx.doi.org/10.5772/intechopen.70952

surface morphology and hardness with the variations in chemical composition and crystallinity after irradiation.

## 2. Experimental setup

KrF excimer laser (EX 200/125-157 GAM Laser, USA) of pulse duration of 20 ns, pulse energy of 70 mJ, repetition rate of 20 Hz, and wavelength of 248 nm was employed for irradiation of Zr targets. The unfocused beam was rectangular with size 11 × 7 mm. The beam was focused by using a circular lens of 50 cm focal length and the focused beam spot appeared elliptical with major and minor axis of 2.5 × 1 mm, respectively.

Zr was bought from Alfa Aesar with purity 99.9%. EDS of the untreated and laser-irradiated samples was performed to check the elemental composition of targets before and after irradiation. **Table 1** shows the wt.% of elements present in untreated and treated samples. Zr targets rectangular in shape (dimensions: 8 × 8 × 2 mm) were grinded and polished to get mirror-like surface in order to decrease the surface roughness and to enhance the quality of the surface. The polished samples were cleaned ultrasonically for 30 minutes with acetone. These polished samples were then placed in quartz cuvette (Cuvette dimensions: 10 × 10 × 45 mm). **Figure 1** shows the schematic diagram of the experimental setup. Threshold fluence for Zr was calculated by using following relation [15].

$$F_{th} = \rho L_v \sqrt{a\, t_{e.}} \tag{1}$$

where "$L_v$" is the specific heat of vaporization per unit mass, "ρ" is the density of sample, "a" is the thermal diffusivity (a = K/ρC, where C and K are the specific heat and thermal conductivity respectively), and $t_e$ is the pulse duration of laser and their values are, ρ = 6.52 g/cm$^3$, $L_v$ = 6375 J/g, a = 0.1246 cm$^2$/s, $t_e$ = 20 ns by substituting the values in above equation, we get the value of threshold fluence, which comes out to be 2.08 J/cm$^2$. Zr targets were exposed for several number of overlapping laser pulses ranging from 500 to 2000, for laser fluence of 3.6 J/cm$^2$, which is higher than the threshold fluence. The ablation threshold fluence is the minimum fluence to generate a surface damage that can be seen under the SEM. For nanostructuring of

| Elements | Untreated (wt. %) | Deionized water (wt.%) | Ethanol (wt.%) |
|---|---|---|---|
| Zr | 87.52 | 70.78 | 74.81 |
| B | 2.78 | 2.75 | 4.08 |
| C | 2.82 | 2.59 | 3.36 |
| O | 4.91 | 21.52 | 15.55 |
| Re | 1.97 | 2.36 | 2.20 |

**Table 1.** The comparative EDX analysis of the unirradiated and central-ablated area of zirconium target after excimer laser irradiation at a fluence of 3.6 J/cm$^2$, wavelength of 248 nm, pulse duration of 20 ns, and repetition rate of 20 Hz for 1000 laser pulses under ambient environments of deionized water and ethanol.

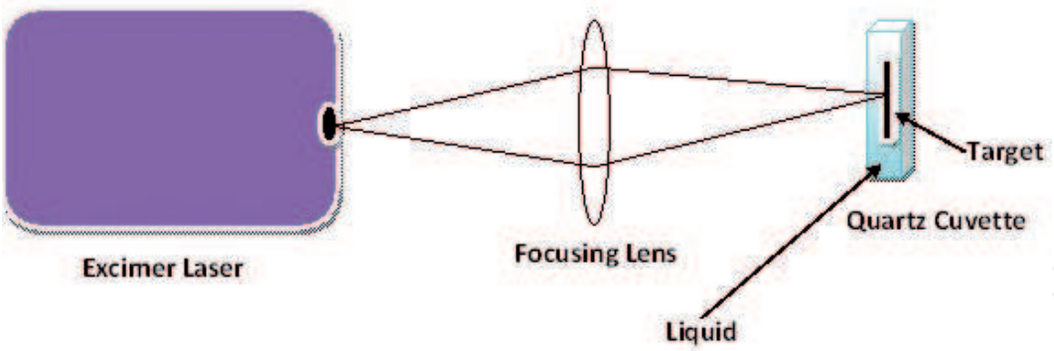


**Figure 1.** Schematic diagram of experimental setup.

materials, fluence should be higher than the threshold fluence and in order to avoid intense heating/melting and burning of the samples, fluence should not be very high.

Absorption coefficient for deionized water has value of $5.05 \times 10^{-3}$/cm [16], whereas for ethanol its value is $4 \times 10^{-2}$/cm [17]. It shows that ethanol will absorb more energy than deionized water; so, less energy will reach the target surface in case of ethanol. This shows that the threshold fluence value will be more for ethanol than deionized water. Experiment was conducted in two steps: (a) nanosecond laser ablation of Zr in ambient environment of deionized water, (b) nanosecond laser ablation of Zr in ambient environment of ethanol. Before exposure to laser, every time fresh liquid was filled in the cuvette with 4 mm thickness over the sample.

To evaluate the crystal structure and phase analysis of the irradiated Zr targets X-ray diffractometer (X'Pert PRO (MPD)) was employed. For chemical analysis, energy dispersive X-ray spectroscopy (EDS-S3700 N) was used. Raman spectroscopic analysis was performed to determine the structural modification of laser-ablated Zr. Scanning electron microscope (SEM-JEOL JSM-6480 LV) was employed to study the surface morphology of ablated targets. Hardness was evaluated by employing the Vickers microhardness tester (HV-1000A).

## 3. Results and discussion

### 3.1. Effect on surface microstructure

**Figure 2** shows the XRD pattern of unirradiated Zr target. Unirradiated sample shows the presence of Zr (100), (002), (101), (102), (110), (103), (004), and (104) plane reflections.

**Figure 3a** represents the XRD diffractograms of laser-irradiated Zr targets, in an ambient environment of deionized water, for varying number of laser pulses ranging from 500 to 2000. **Figure 3b** shows the variation in crystallite size and residual stresses with increase in number of laser pulses. New phases of Zr oxides (zirconia): $ZrO_2$ (−111) (111), (212), (321), (220), $Zr_3O$ (201), (200), (217) and Zr hydrides: $ZrH_2$ (112), ZrH (123) are also detected together with the original phases of Zr.

http://dx.doi.org/10.5772/intechopen.70952

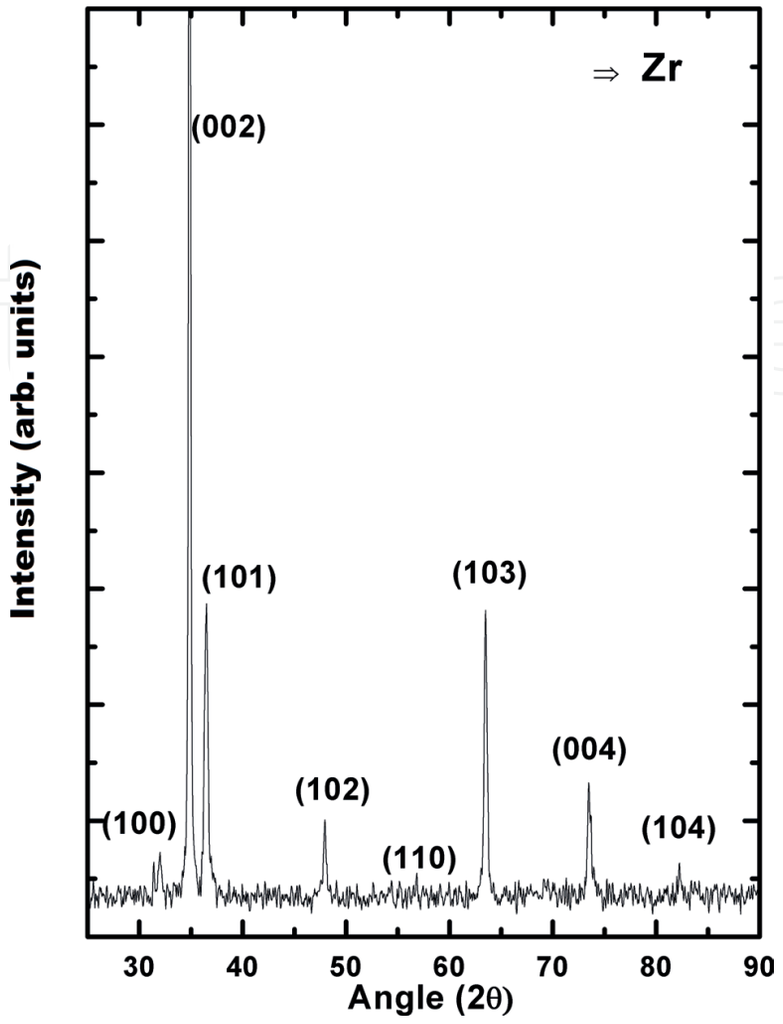


**Figure 2.** XRD patterns of unirradiated zirconium.

For $ZrO_2$ (212) plane reflection, the crystallite size is calculated by using Scherrer's formula [18].

$$\text{Crystallite Size (D)} = \frac{0.9\,\lambda}{\text{FWHM}\cos\theta} \tag{2}$$

where D is crystallite size, $\lambda$ is the wavelength of X-rays (1.5406 Å), FWHM is full width at half maximum, and $\theta$ is the angle of diffraction.

Following relation is used to evaluate the residual strains [18].

$$\text{Strain } (\varepsilon) = \frac{d - do}{do} \tag{3}$$

where d is the observed, $d_0$ is the standard plane spacing, and $\varepsilon$ is the induced strain.

By using the relation given below, the induced stresses are calculated

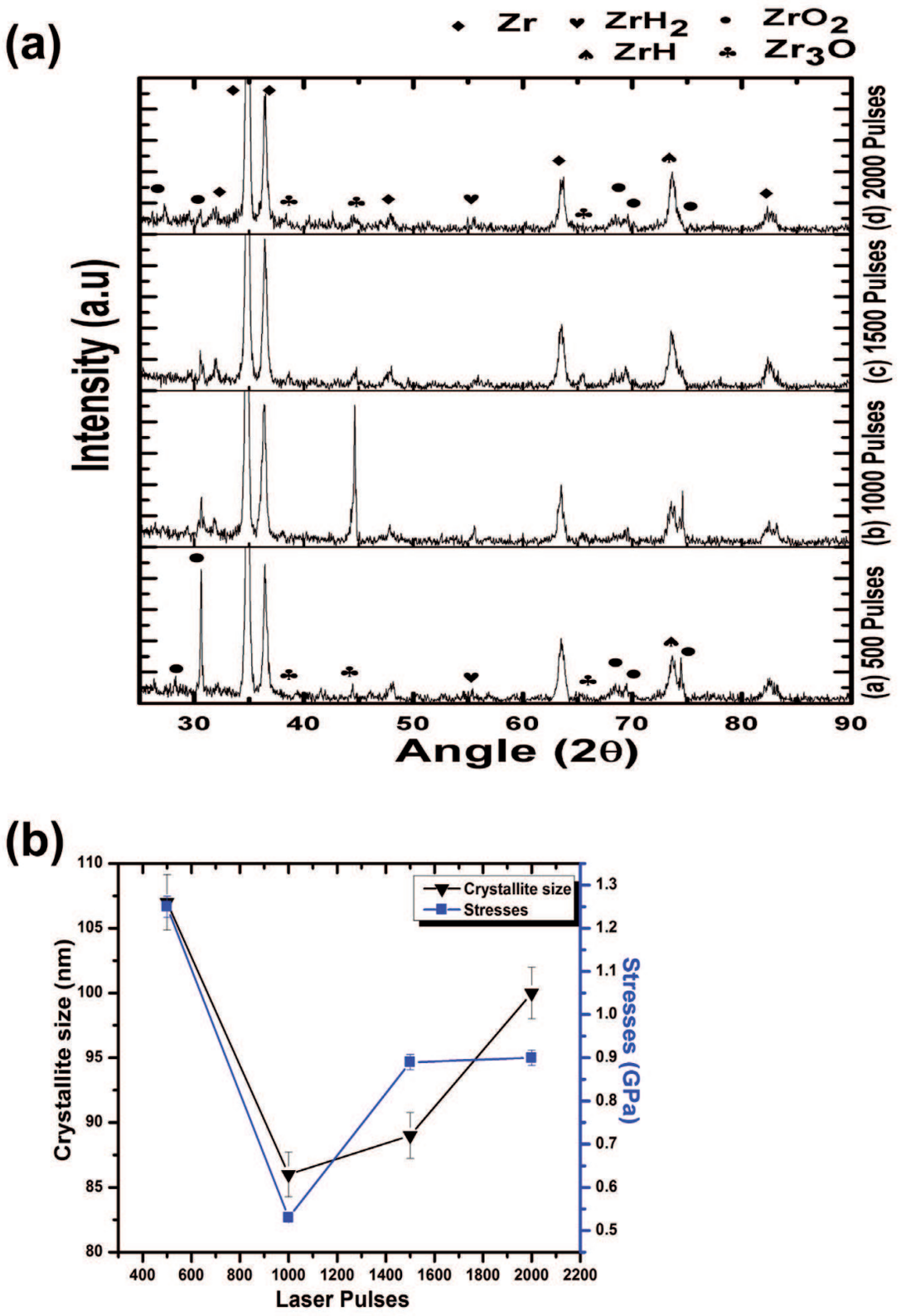


**Figure 3.** (a) XRD patterns of excimer laser-irradiated zirconium samples, (b) variation in the crystallite size and residual stresses of laser-irradiated zirconium for various number of overlapping laser pulses in an ambient environment of deionized water.

http://dx.doi.org/10.5772/intechopen.70952

$$\text{Stress } (\sigma) = \varepsilon E \tag{4}$$

where ε is the strain, E is the young's modulus for $ZrO_2$ and its value is 186.21 GPa [19].

Intensity of peak and crystallite size of $ZrO_2$ (212) reflection plane first decreases and then increases with increase in number of laser pulses, **Figure 3a, b**. Initial reduction in the intensity of peak is due to the recrystallization of the irradiated targets during resolidification after melting.

After irradiation with laser, the larger crystallites breakup into smaller ones (**Figure 3b**) that also results in decrease in peak intensity [20]. The decrease in size of the crystallites is also credited to the interstitial diffusion of the gas atoms, which causes the peak broadening owing to the variation of d-spacing [21]. The ablated Zr atoms chemically react with atoms of the surrounding gas (oxygen/hydrogen) and redeposit on the target surface after the formation of oxides and hydrides. Formation of theses oxides and hydrides is attributable for the decrease in crystallite size [22]. The possible defect production and growth of residual stresses might also be considered to be other reasons for decrease in the crystallite size [22]. An increase in stacking faults and structural disorder owing to the diffusion of hydrogen/oxygen widens the XRD peaks [23]. Increases in density of point defects affect the crystallinity and grain boundary mobility, which in turns causes a linear increase in the FWHM of XRD peak. The increase in intensity of the peak and crystallinity of $ZrO_2$ (212) reflection plane is due to the increased oxygen diffusion into the surface across the boundaries of grains and enhancement in the X-ray's diffraction from the surface of the target [24]. The diffusion of oxygen in Zr after irradiation is exhibited in EDX analysis depicted in **Table 1**. The microstructure and Bragg's conditions of diffraction of Zr surface gets modified after the interaction with nanosecond laser. These variations in the microstructure and Bragg's conditions of diffraction are attributable to the variation in d-spacing and intensity of diffraction lines. The variation in laser-induced residual stresses for a variety of number of laser pulses is exhibited in **Figure 3b**.

Laser-induced thermal shocks and lattice defects generated by oxygen ions incorporation into the lattice may cause residual stress variation. Compressive stresses are generally due to ion implantation, whereas laser-induced thermal shocks are responsible for tensile stresses [25]. For 500 number of laser pulses, high tensile stresses are present, which relax on increase in number of laser pulses to 1000. The defects and stresses produced by initial pulses are annealed and relaxed after successive pulses. When number of pulses are increased up to a value of 2000, thermally induced shocks results into increasing tensile stresses [24].

XRD patterns displayed in **Figure 4a** confirms the presence of oxides (zirconia) and hydrides of zirconium after irradiation in an ambient environment of ethanol for various number of overlapping laser pulses of (a) 500, (b) 1000, (c) 1500, and (d) 2000. New phases of zirconium oxides (zirconia): $ZrO_2$ (111), (212), (321), (114), $Zr_3O$ (201), $Zr_3O$ (217), and zirconium hydrides: ZrH (123) and $ZrH_2$ (112) (appeared after 1000 laser pulses) are observed along with the original phases of zirconium.

Decrease in intensity (**Figure 4a**) and crystallinity (**Figure 4b**) of $ZrO_2$ (212) plane reflection is observed with increasing number of laser pulses up to 2000. Decrease in peak intensity and

crystallite size is attributable to interstitial diffusion of oxygen atoms/ions. Interstitial diffusion of oxygen atoms/ions induces microstrain defects and these induced defects causes an increase in FWHM and reduction in the peak intensity and crystallite size.

**Figure 4b** also represents variation in induced stresses of zirconium after irradiation with various number of laser pulses. For 500 number of laser pulses, tensile stresses are observed. They relax with increasing number of laser pulses up to 2000. This relaxation is due to reduction in crystallite size. Diffusion of oxygen/hydrogen atoms into the surface causes the decrease in crystallite size and hence causes the highly tensile stresses to be relaxed.

Comparison of XRD data of ablated zirconium in deionized water (**Figure 3**) and ethanol (**Figure 4**) shows the presence of oxides (zirconia) and hydrides of zirconium for both media.

Energy dispersive X-ray spectroscopy (EDS) was carried out for chemical analysis of unirradiated and irradiated zirconium targets. Unirradiated sample shows following contents: zirconium ~ 87.52 wt.%, balanced to 100% by B (~2.78 wt.%), C (~2.82 wt.%), O (~4.91), Re (~1.97 wt.%). **Table 1** shows the comparative EDX analysis of the unirradiated and central-ablated area of Zr target after excimer laser irradiation under ambient environments of deionized water and ethanol. The increase in the content of oxygen from 4.91 wt.% to a value of 21.52 wt.% is observed in case of deionized water, whereas less diffusion of oxygen (15.55 wt.%) but increase in content of carbon from 2.82 to 3.36 wt.% is observed in case of ethanol. Multipulse irradiation induced heating of Zr causes efficient diffusion of atomic oxygen/carbon into the target surface; therefore, oxides and carbides are formed [26].

**Figure 5a, b** shows the Raman spectra of Zr samples irradiated for various number of laser pulses at a fluence of 3.6 J/cm$^2$ in ambient environments of deionized water and ethanol. Raman modes arise after laser ablation of Zr due to the formation of oxides and hydrides of Zr on the metallic surface.

For deionized water (**Figure 5a**), Raman peaks identified at 320, 337 cm$^{-1}$ represents the Zr—Zr bond. Peak identified at 535 cm$^{-1}$ corresponds to O—O bond [27], while peaks appearing at 363, 372, 420, 480, and 640 cm$^{-1}$ are characteristic bands of monoclinic $ZrO_2$ [28] and the peak identified at 269 cm$^{-1}$ can be assigned to the presence of tetragonal $ZrO_2$ [29]. The inset of **Figure 5a** represents the identified peak of zirconium hydride (ZrH) at 1597 cm$^{-1}$.

**Figure 5b** represents Raman spectra for ethanol environment. Peaks identified at 351, 422, and 538 cm$^{-1}$ correspond to monoclinic $ZrO_2$ [28]. Raman peaks identified at 269 and 312 cm$^{-1}$ can be assigned to the presence of tetragonal $ZrO_2$ [29]. Peak identified at 476 corresponds to O—O bond [27]. The inset of **Figure 5b** represents identified peak of C═O at 1760 cm$^{-1}$.

The Zr samples after irradiation in deionized water and ethanol consist of a mixture of monoclinic and tetragonal $ZrO_2$ phases. The presence of hydride is confirmed from Raman spectra of samples irradiated in deionized water and the presence of carbon diffusion is confirmed only in case of ethanol. These Raman results are in good agreement with the EDS and XRD results.

http://dx.doi.org/10.5772/intechopen.70952

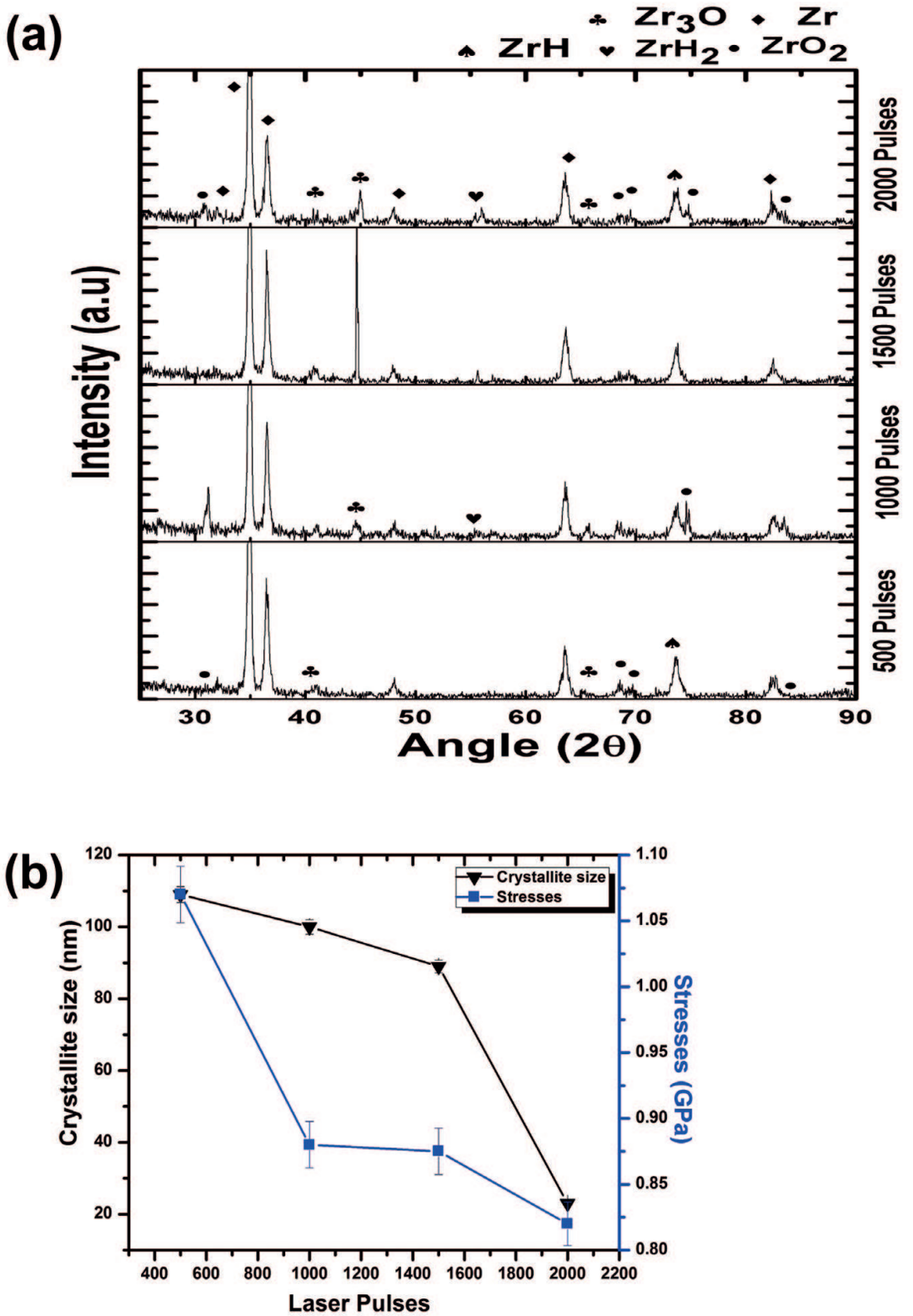


**Figure 4.** (a) XRD patterns of excimer laser-irradiated zirconium samples, (b) variation in the crystallite size and stresses of laser-irradiated zirconium for various number of overlapping laser pulses in an ambient environment of ethanol.

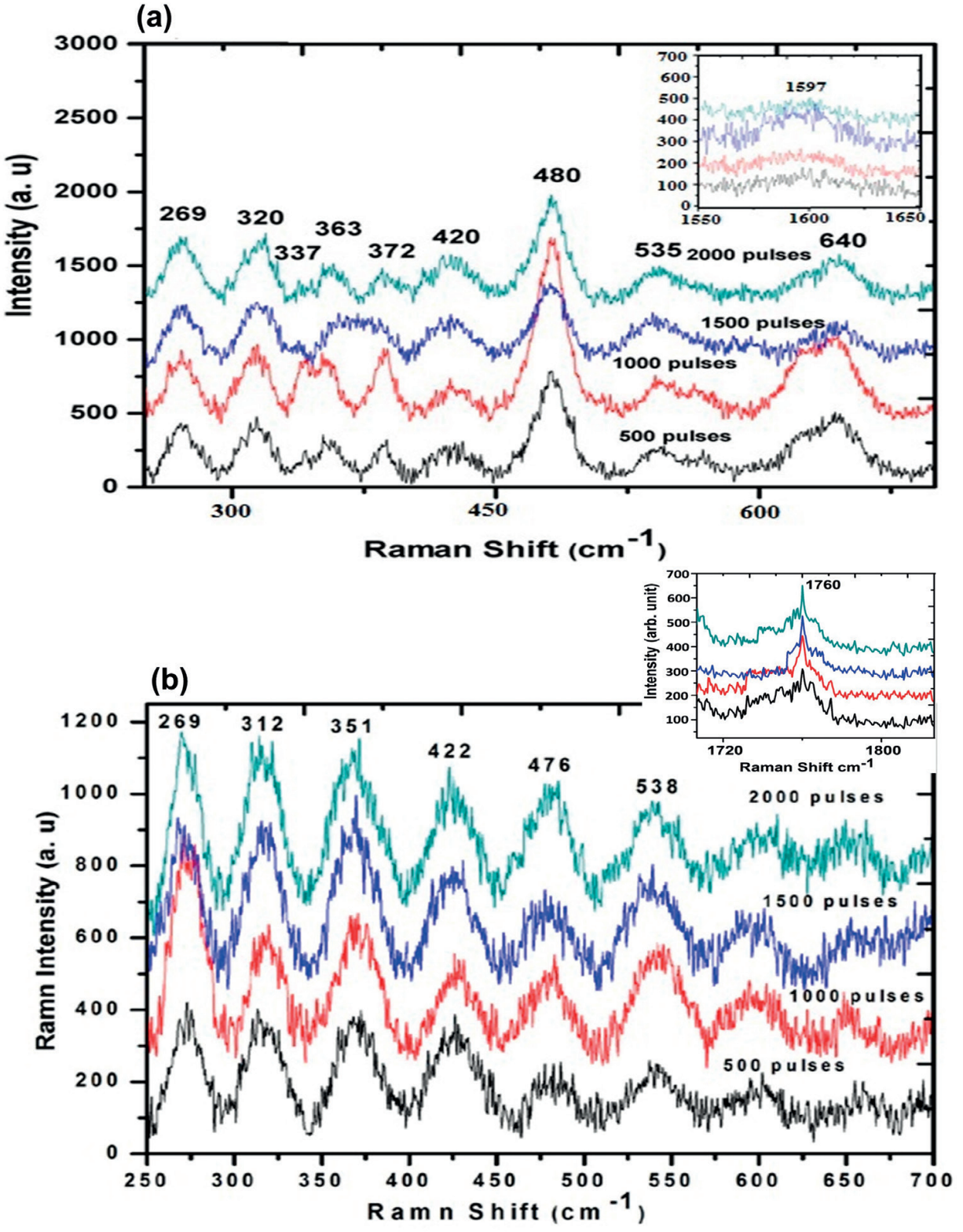


**Figure 5.** Raman spectroscopy analysis of excimer laser-irradiated zirconium in an ambient environment of (a) deionized water, (b) ethanol.

http://dx.doi.org/10.5772/intechopen.70952

### 3.2. Effect on surface morphology

**Figure 6a–e** represents the surface morphology of Zr sample after irradiation with various number of overlapping laser pulses at fluence of 3.6 J/cm$^2$ in an ambient environment of deionized water.

**Figure 6a** exhibits the surface morphology of Zr sample after irradiation with 500 laser pulses. No significant redeposition of the material around the edges of the craters is observed because the ablated species are taken away by the surrounding liquid. Rapid temperature rise during laser-induced plasma expansion/formation generates bubbles in the liquid. The bubble motion is responsible for the removal of ablated particles and hence no redeposition on the target surface is observed [30]. The liquid has played considerable role in ablation of Zr and it effectively cools the target preventing the excessive heat accumulation after laser irradiation.

**Figure 6b–e** reveals enlarged SEM images of the central-ablated area of Zr in an ambient environment of deionized water for various number of pulses, that is, (b) 500, (c) 1000, (d) 1500, and (e) 2000. **Figure 6b** reveals the uniform distribution of large number of droplets over the porous surface. Small-sized cavities and cracks are also present with some signs of melting. Further increase in laser pulses up to 1000, few large-sized droplets along with cavities are revealed (**Figure 6c**). No cracks are observed for 1000 laser pulses. For 1500 number of laser pulses, density of pores and cracks increases significantly (**Figure 6d**). For 2000 number of pulses, highly porous surface is observed, whereas the droplets and cavities are completely vanished (**Figure 6e**).

Pulsed laser irradiation of Zr in liquid-confined environment creates high temperature and high pressure plasma, and consequently, high density of excited electrons. These electrons transport their energy to phonons during electron–phonon relaxation. The energy is redistributed during lattice vibrations and as a result, heat is conducted in the Zr target. This heat might melt or vaporize the sample. It is worth noting that the surface morphology of the irradiated Zr consists of large number of pores and cavities. An explosive melt expulsion in the confined environment could be a prevailing process for the laser ablation of Zr in deionized water [31]. These results are well correlated with the change in the crystallinity of the irradiated samples. For 500 number of laser pulses, highly tensile stresses are present (**Figure 3b**), which are responsible for the presence of cavities and pores over the surface. For 1000 pulses, refilling of cavities by melted and shock-liquefied material causes vanishing of pores and cavities representing the relaxation in tensile stresses [32]. For 2000 laser pulses, highly porous surface shows the presence of enhanced tensile residual stresses after irradiation (**Figure 3b**).

**Figure 7** represents the surface morphology of overall and central-ablated area of Zr samples after irradiation with various overlapping numbers of laser pulses at 3.6 J/cm$^2$ in an ambient environment of ethanol. **Figure 7a** is an overall view of ablated area exposed to 500 laser pulses. Appearance of the overall ablated area is less distinct or faint as compared to

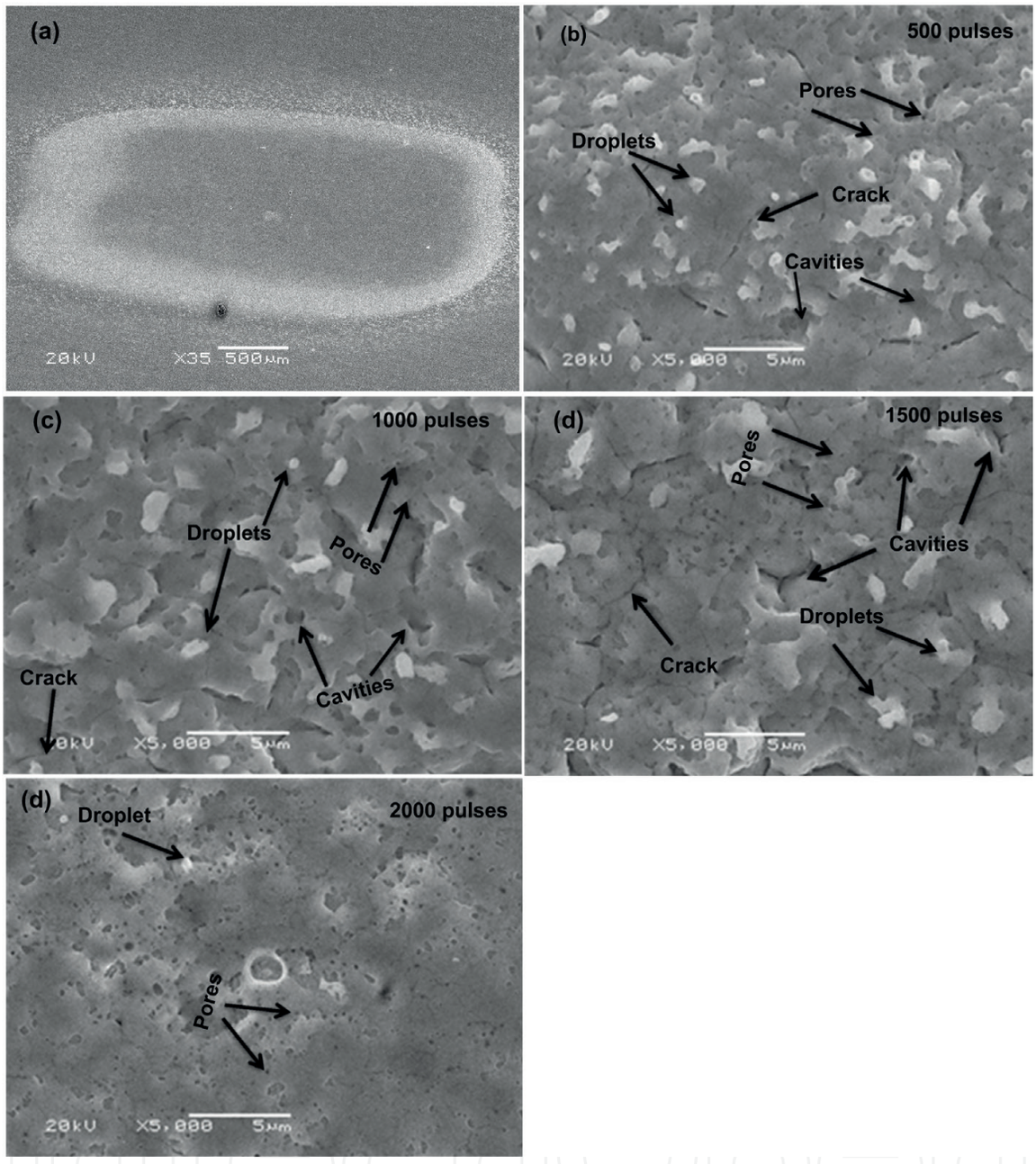


**Figure 6.** SEM images revealing the surface morphology of (a) overall view of the ablated crater after excimer laser irradiation with 500 laser pulses at a fluence of 3.6 J/cm$^2$, (b–e) magnified SEM images of central-ablated area revealing the variation in surface morphology of zirconium after irradiation under ambient environment of deionized water for various number of overlapping laser pulses, that is, (b) 500, (c) 1000, (d) 1500, and (e) 2000.

the overall image of ablation spot in case of deionized water. From literature, the observed values of absorbance and absorption coefficient are 0.00086 and $5.05 \times 10^{-3}$/cm for deionized water [16], whereas 0.0055 and $4 \times 10^{-2}$/cm for ethanol [17]. This difference in the appearance of ablation spot is attributable to more absorption of energy (0.0055) by ethanol, then deionized water.

http://dx.doi.org/10.5772/intechopen.70952

**Figure 7b–e** reveals enlarged view of SEM images of the central-ablated area of Zr in an ambient environment of ethanol for various number of pulses, that is, (b) 500, (c) 1000, (d) 1500, and (e) 2000. **Figure 7b** represents granular morphology with distinct grain boundaries with average grain size of 2.20 μm. With increase in the number of laser pulses up to 1000 increase in size of grains up to 3.06 μm is observed with distinct and wider boundaries (**Figure 7c**). Further increase in number of pulses up to 1500 shows globules instead of distinct grains. The presence of cracks and large number of pores is also evident (**Figure 7d**). For 2000 number of laser pulses, material segregates into distinct grains with average grain size of 3.26 μm and much wider grain boundaries (**Figure 7e**).

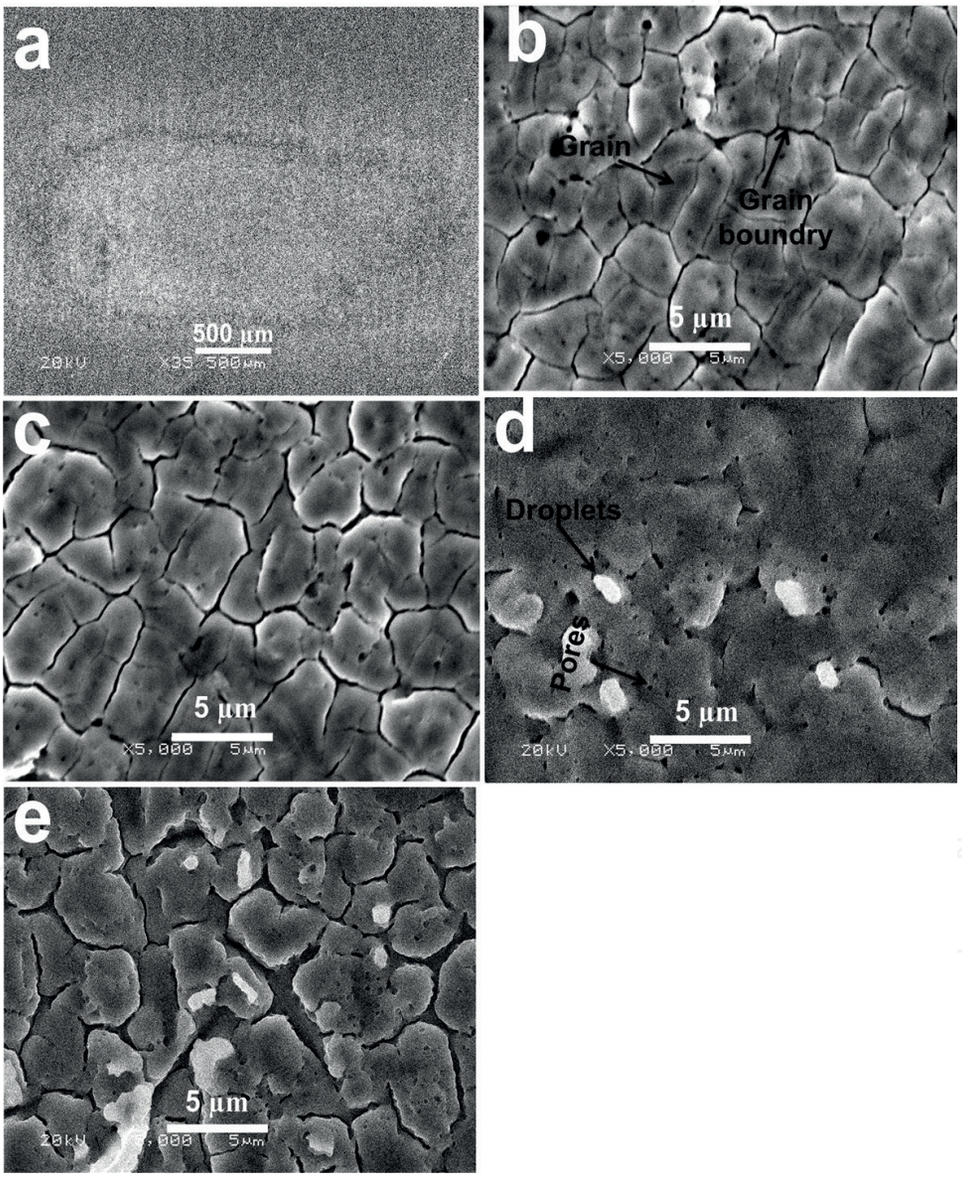


**Figure 7.** Magnified SEM images of excimer laser-irradiated zirconium at a fluence of 3.6 J/cm$^2$ (a) overall view of sample irradiated with 500 overlapping pulses (b–e) Magnified SEM images of central-ablated area revealing the variation in surface morphology of zirconium after irradiation under ambient environment of ethanol for various number of overlapping laser pulses, that is, (b) 500, (c) 1000, (d) 1500, and (e) 2000.

Laser-induced heating and cooling, the temperature gradient, and laser-induced residual stresses are responsible for growth of such grains [26]. When the laser pulse is over, the molten material generated by fast heating is supercooled and acts as an effective heat sink that quickly removes any released latent heat and causes the crystal growth. The presence of pores and cracks across the grain boundaries confirms the presence of tensile residual stresses after ablation in ethanol environment.

The presence of various crystal planes is property of the material. Variations in surface morphology can be related to the motion of the crystal planes after laser irradiation due to the production of defects owing to diffusion, which causes the formation of various new crystal planes ($ZrO_2$, $Zr_3O$, ZrH, $ZrH_2$, etc). During irradiation, diffusion of oxygen/carbon/hydrogen caused the increase in density of point defects, stacking faults, and structural disorder, which results in higher angle shifting of planes, which causes the production of compressive stresses. Laser-induced thermal shock causes the peak shift to lower angular position, which confirms the production of tensile residual stresses [25]. Variations in stresses are responsible for the production of various type of surface features, for example, cavities, pores, cracks, droplets, bumps, hillocks, protrusion, etc. after irradiation [21].

In case of ethanol, tensile stresses are present for all laser pulses (from 500 to 2000), but their behavior is not in agreement with the surface morphology especially for 1500 number of laser pulses. We have calculated stress variations for only one plane, that is, $ZrO_2$ (212). But other phases also play role for surface modification after irradiation, for example, with the increase of number of pulses from 500 to 1000 formation of new phases ($Zr_3O$, $ZrH_2$, $ZrO_2$) is observed due to the enhanced diffusion of oxygen/hydrogen across the grain boundaries, which results in increase in grain size (**Figure 7b**) along with wider grain boundaries. For further increase of number of pulses from 1000 to 1500, some peaks get demolished ($ZrO_2$, $Zr_3O$), whereas growth of some other phases (ZrH, $ZrH_2$, $Zr_3O$) is observed on the target surface. This shows that energy transferred to the target surface after 1500 number of laser pulses causes the laser annealing on target surface. After laser annealing during recovery process, rapid cooling due to the presence of surrounding liquid, some phases do not get sufficient energy to grow, whereas some of them get to grow. This is the reason for different structures over the surface for 1500 pulses (**Figure 7c**, subsurface boiling, globules, pores, and cracks). For 2000 number of pulses after annealing, due to recrystallization phenomena reduction in peak intensity and increase in FWHM, is observed for almost all phases along with the growth of demolished phases due to the diffusion of oxygen/hydrogen across the boundaries is observed. This variation is responsible for further variation in surface morphology of irradiated zirconium (**Figure 7e**).

Laser-induced rapid heating, cooling, and a large temperature gradient are considered to be responsible for grain growth. Grain growth occurs as a result of the recrystallization process, which arises during irradiation in order to minimize the absorbed strain and surface energy. The inter planar atomic motion reorients the lattice at the expense of this energy, which leads to the growth of large and smooth grains [33]. Cavities are formed by the liberation of adsorbed gases beneath the surface during laser irradiation, due to volume boiling [34].

http://dx.doi.org/10.5772/intechopen.70952

Melting of the target surface after laser irradiation activates reaction between the molten surface and surrounding media. After laser irradiation, recrystallization takes place and oxygen, carbon//hydrogen disseminates into the surface (oxygen insertion is confirmed by EDS analysis and hydrogen diffusion is confirmed by XRD analysis) particularly at the grain boundaries, attack and weaken them. The attacked and weakened grain boundary in turn enhances the effect of tensile stress and causes the widening of the grain boundaries [35]. Successive heating by overlapping laser pulses enhances diffusion of oxygen/hydrogen into the molten surface and causing the formation of oxides and hydrides of Zr (confirmed from XRD analysis) [26].

Comparison of two media, deionized water (**Figure 6**) and ethanol (**Figure 7**), shows significant dissimilarities. For laser ablation in deionized water porous surface features are observed with large number of pores and cavities over the surface. For ethanol distinct, well defined and small-sized grains are developed. This difference in surface morphology is attributable to the difference in absorption offered by the liquids and difference in chemical reactivity of Zr with both liquids. During irradiation of Zr in liquid environment, plasma plume from the solid target will be generated at the solid-liquid interface and remains confined. A shock wave is created in the plasma plume by the laser-induced plasma due to the confinement of liquid. This shock wave will induce an extra pressure in the laser-induced plasma called plasma-induced pressure [36]. The plasma-induced pressure will lead to an additional temperature increase of the laser-induced plasma. Therefore, the shock wave generated by the expansion of laser-induced plasma, under confinement of liquid pushes the laser-induced plasma into a thermodynamic state of the higher temperature, higher pressure and higher density, and the plume species react with surrounding liquid molecules in this extreme state to form various compounds like $ZrO_2$ (tetragonal and monoclinic), $Zr_3O$, ZrH, and $ZrH_2$ [37].

Intermolecular forces determine the physical and chemical characteristics of a substance, such as boiling and melting points, viscosity, solubility, volatility, and surface tension. Ethanol ($C_2H_6O$) is more volatile than water ($H_2O$), and it boils at a much lower temperature (78.24°C) than water (100°C). The strength of the intermolecular forces in ethanol is much less than water. In water, intermolecular hydrogen bonding takes place due to the presence of highly polar O—H bond in the $H_2O$ molecule. Ethanol can also participate in hydrogen bonding, but not as successfully as water because it has a non-polar region. Heat of vaporization of water is 44 kJ/mol and its vapor pressure is 3.17 kPa at 25°C, whereas for ethanol, the value of heat of vaporization is 38.56 kJ/mol and its vapor pressure is 5.95 kPa at 25°C. The molar mass of water is 18 g/mol and for ethanol, its value is 46.07 g/mol, which is more than twice the mass of water that means, when 1 g of water evaporates, it absorbs more than two times as much heat as 1 g of ethanol evaporating. So, ethanol boils at a lower temperature than water, and its equilibrium vapor pressure is higher at all temperatures. That is why ethanol is more volatile than water and is responsible for the formation of various compounds of Zr. Physical properties of both liquids are mentioned in **Table 2**.

XRD and Raman results reveal the formation of zirconium oxide ($ZrO_2$, $Zr_3O$), zirconium hydride (ZrH, ZrH2) in case of ablation in deionized water and ethanol. Diffusion of carbon

| Physical properties of liquids | | |
|---|---|---|
| **Properties** | **Deionized water** | **Ethanol** |
| Melting point | 0°C | −114.14°C |
| Boiling point | 100°C | 78.24°C |
| Viscosity | 0.890 mPa·s | 1.074 mPa·s |
| Density | 0.9970474 g/cm$^3$ | 0.7893 g/cm$^3$ |
| Refractive index | 1.3330 | 1.3611 |
| Heat of vaporization | 44 kJ/mol | 38.56 kJ/mol |
| molar mass | 18 g/mol | 46.07 g/mol |
| Absorption coefficient | $5.05 \times 10^{-3}$/cm | $4 \times 10^{-2}$/cm |
| Vapor pressure | 3.17 kPa (at 25°C) | 5.95 kPa (at 25°C) |
| Strength of the intermolecular forces | High due to presence of highly polar O—H bond | Low due to presence of nonpolar region |
| Volatility | Low | High |

**Table 2.** Physical properties of liquids (deionized water and ethanol).

along with oxygen (C═O) is only confirmed through the Raman analysis of samples ablated in ethanol environment (EDS supports the results of XRD and Raman, it confirmed the diffusion of oxygen in case of deionized water and diffusion of oxygen/carbon in case of ethanol). Pulsed laser ablation in liquid is an extremely nonequilibrium process. When the nanosecond laser pulses interact with Zr at the liquid-solid interface, the absorption is granted by electrons in the metal. In terms of time scaling, absorption takes place after $10^{-14}$ s. The hot carriers can transfer their energy to the target lattice leading eventually to a solid-liquid phase transition. This energy transfer leads to an equilibrium on a timescale, $\tau E = 10^{-12} - 10^{-11}$ s and the mass removal will occur from equilibrium phase transition [38]. The ejected species will have large kinetic energy after irradiation and a plasma plume is formed at the interface. The plasma plume expands adiabatically while the liquid confines it. The confinement effect of liquids result in much higher temperature and pressure inside the plasma plume [37] and the plume species react with the surrounding liquid molecules in this extreme state. Moreover, the cooling effect of the liquids cause quenching of the plasma plume and the plume species solidifies to preserve materials in the final yield. In our case zirconium oxide $ZrO_2$ (monoclinic and tetragonal phases), $Zr_3O$, and zirconium hydride (ZrH, $ZrH_2$) in case of ablation in both deionized water and ethanol, whereas in case of ethanol C═O are synthesized and redeposited over the surface after fast quenching of the plasma plume at room temperature. Furthermore, the laser energy absorption in case of deionized water is less than ethanol. High absorption in ethanol for 248 nm laser than water implies small rise in surface temperature during irradiation, which supports grain growth. In case of water due to

http://dx.doi.org/10.5772/intechopen.70952

less energy absorption for 248 nm laser, average rise in surface temperature will be high, which causes the melting and resolidification of Zr targets. This results in the formation of cavities, pores, cracks, and droplets over the surface after irradiation. The strength of the intermolecular forces in ethanol is much less than water, that is why ethanol is more volatile than water and is responsible for the diffusion of carbon along with hydrogen and oxygen. The observed diffusion of carbon may also be responsible for different structure in case of ablation in ethanol.

Moreover, the cooling effect of the liquids causes quenching of plasma plume and the plume species will be redeposited over the target surface. This is the reason for variation in concentration of various elements after ablation as compared to unirradiated Zr (EDS analysis, **Table 1**). The formation of $ZrO_2$ (monoclinic and tetragonal phases), $Zr_3O$, and zirconium hydride (ZrH, $ZrH_2$) in case of ablation in both liquids and formation of C═O in case of ethanol plays considerable role in the formation of various microstructures. During exposure in liquid environments, the sample surface gets cooled in the presence of liquids, which results in less pronounced thermal effects and the surface morphologies become much cleaner and smoother.

### 3.3. Effect on surface mechanical property

Untreated Zr sample shows hardness value of 850 MPa. **Figure 8** shows the variation in hardness of nanosecond laser-irradiated Zr targets as a function of increasing number of laser pulses. **Figure 8a** shows the variation in hardness after irradiation with nanosecond laser in ambient environment of deionized water. For 500 laser pulses, hardness value of 964 MPa is observed, which increases (up to 1125 MPa) with increase in number of laser pulses up to 1000. Further increase in number of laser pulses up to 2000 shows continuous decrease in hardness (up to 995 MPa).

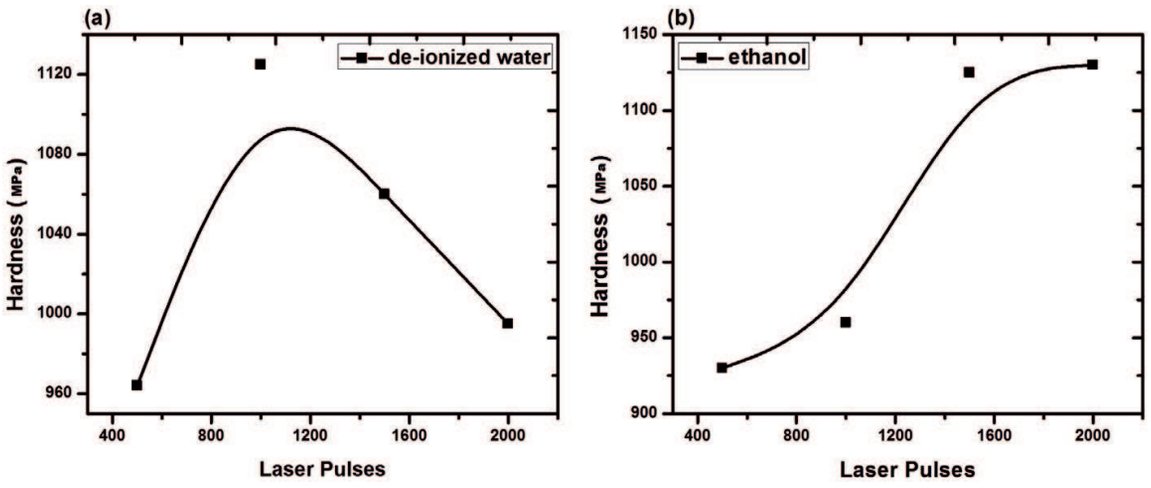


**Figure 8.** The variation in microhardness of excimer laser-irradiated zirconium in ambient environment of (a) deionized water and (b) ethanol.

Variations in the value of hardness depend on a number of factors including the lattice defects, density of oxide contents, phase composition, size and distribution of grains and crystal structure [39]. Increase in hardness is attributable to interstitial diffusion of oxygen into the lattice, which results in decrease in crystallite size and tensile residual stresses (**Figure 3b**) [40]. Smaller crystallite size is efficient in obstructing the dislocation movement and is responsible for high strength and hardness. Decrease in value of hardness, of irradiated targets can be explained on the basis of increasing crystallite size and enhanced tensile residual stresses. Oxygen diffusion across the grain boundaries results in larger crystallites (**Figure 3b**) that are more prone to coarsening, leading to lower crystallite density, and hence lower hardness [40, 41].

**Figure 8b** shows the variation in surface hardness after irradiation in ambient environment of ethanol. For 500 number of laser pulses, hardness of 960 MPa is observed, which increases with the increase in number of laser pulses up to 2000 (up to 1130 MPa).

## 4. Conclusion

The structural modifications of KrF excimer laser-ablated Zr has been investigated in correlation with its surface and mechanical properties after ablation in ambient environments of deionized water and ethanol. Both ambient environments have played significant role in structural, chemical, and mechanical modifications of the irradiated zirconium surface.

XRD results show diffusion of oxygen and hydrogen into the surface, which cause the formation of $Zr_3O$, monoclinic, and tetragonal phases of zirconium oxide ($ZrO_2$) and hydrides of zirconium (ZrH, $ZrH_2$) on the metallic surface. EDS analysis confirmed the increase in content of oxygen for both liquids. Raman analysis supports the EDS and XRD results. It confirms the formation of zirconia and hydrides of zirconium after ablation. The presence of liquids helps in removing the ablation debris and reducing the thermal damages, and offered cleaner surface during laser ablation of Zr. As a result, the surface morphologies of the craters produced are much smoother. For ablation in deionized water, porous surface morphology is observed for whole range of laser pulses, whereas fine grains are formed in case of ethanol environment. Formation of $ZrO_2$ (monoclinic and tetragonal phases), $Zr_3O$, and zirconium hydride (ZrH, $ZrH_2$) in case of ablation in both liquids and formation of C═O in case of ethanol and different absorption offered by both liquids plays considerable role in the formation of various microstructures. Different interacting mechanisms such as recoil pressures, production of bubbles, and laser-induced surface melting of Zr also plays considerable role in the formation of various microstructures. First, increase and then decrease in hardness is observed in case of deionized water, whereas continuous increase in hardness is observed for ethanol. Variations in hardness depend on a number of factors including the lattice defects, density of oxide contents, phase composition, size and distribution of grain, and crystal structure.

http://dx.doi.org/10.5772/intechopen.70952

## Author details

Nisar Ali[1,3,4]*, Umm-i-Kalsoom[2,3,4], Shazia Bashir[3] and Narjis Begum[5]

*Address all correspondence to: chnisarali@gmail.com

1 Department of Basic Sciences and Humanities, University of Engineering and Technology Lahore, Faisalabad, Pakistan

2 Department of Basic Sciences and Humanities, University of Engineering and Technology Lahore, Lahore, Pakistan

3 Centre for Advanced Studies in Physics, GC University, Lahore, Pakistan

4 Department of Physics, GC University, Lahore, Pakistan

5 Department of Physics, COMSATS Institute of Information Technology, Islamabad, Pakistan

## References

[1] Barmina EV, Serkov AA, Stratakis E, Fotakis C, Stolyarov VN, Stolyarov IN, Shafeev GA. Nano-textured W shows improvement of thermionic emission properties. Applied Physics A. 2012;**106**:1

[2] Yang Y, Yang J, Liang C, Wang H. Ultra-broadband enhanced absorption of metal surfaces structured by femtosecond laser pulses. Optical Express. 2008;**16**:11259-11265

[3] Vorobyev AY, Makin VS, Guo C. Brighter light sources from black metal: Significant increase in emission efficiency of incandescent light sources. Physics Review Letters. 2009;**102**:234301

[4] Yang Y, Yang J, Liang C, Wang H, Zhu X, Zhang N. Surface microstructuring of Ti plates by femtosecond lasers in liquid ambiences: A new approach to improving biocompatibility. Optics Express. 2009;**17**:21124

[5] Bekesi J, Kaakkunen J, Michaeli W, Klaiber F, Schoengart M, Ihlemann J, Simon P. Fast fabrication of super-hydrophobic surfaces on polypropylene by replication of short-pulse laser structured molds. Applied Physics A. 2010;**99**:691

[6] Bonse J, Koter R, Hartelt M, Spaltmann D, Pentziea S, Höhm S, Rosenfeld A, Krüger J. Tribological performance of femtosecond laser-induced periodic surface structures on titanium and a high toughness bearing steel. Applied Surface Science. 2015;**336**:21

[7] Jelani M, Bashir S, Akram M, Yousaf D, Afzal N, Ahmad S. Mechanical behaviour of excimer laser irradiated polycrystalline zirconium. Physica Scripta. 2014;**89**:025703-025710

[8] Bashir S, Rafique MS, Husinsky W. Liquid assisted ablation of zirconium for the growth of LIPSS at varying pulse durations and pulse energies by femtosecond laser irradiation. Nuclear Instruments and Methods in Physics Research B. 2015;**349**:230

[9] Umm-i-Kalsoom S, Bashir N, Ali M, Rafique S, Husinsky W, Nathala CSR, Makarov SV, Begum N. Effect of fluence and ambient environment on the surface and structural modification of femtosecond laser irradiated Ti. Chinese Physics B. 2016;**25**(1):0181011-0181017

[10] Bashir S, Rafique MS, Nathala CS, Husinsky W. Surface and structural modifications of titanium induced by various pulse energies of a femtosecond laser in liquid and dry environment. Applied Physics A. 2014;**114**:243

[11] Major A, Aitchison JS, Smith PWE, Druon F, Georges P, Viana B, Aka GP. Applied Physics B: Lasers and Optics. 2005;**80**:199-201

[12] Barminaa EV, Stratakis E, Barberoglou M, Stolyarove VN, Stolyarove IN, Fotakisb C, Shafeev GA. Laser-assisted nanostructuring of tungsten in liquid environment. Applied Surface Science. 2012;**258**(15):5898-5902

[13] Ren J, Kelly M, Heeselink L. Laser ablation of silicon in water with nanosecond and femtosecond pulses. Optics Letters;**2005**(30):1740-1742

[14] Bashir S, Vaheed H, Mahmood K. Nanosecond pulsed laser ablation of brass in a dry and liquid-confined environment. Applied Physics A. 2013;**110**(2):389-395

[15] Cabalin LM, Lasema JJ. Experimental determination of laser induced break-down thresholds of metals under nanosecond Q-switched laser operation. Spectrochimica Acta B. 1998;**53**:723-730

[16] Park HK, Kim D, Grigoropoulos CP, Tam AC. Pressure generation and measurement in the rapid vaporization of water on a pulsed-laser-heated surface. Journal of Applied Physics. 1996;**80**(7):4072-4081

[17] Duley WW. UV Lasers: Effects and Applications in Materials Science. New York, United States of America: Cambridge University Press; 2005

[18] Ashraf M, Akhtar SMJ, Khan AF, Ali Z, Qayyum A. Effect of annealing on structural and optoelectronic properties of nanostructured ZnSe thin films. Journal of Alloys and Compounds. 2011;**509**(5):2414-2419

[19] Shackelford JF, Alexander W. CRC Materials Science and Engineering Handbook. 3rd ed. California, USA: CRC Press; 2000

[20] Rafique MS, Khaleeq-ur-Rehman M, Firdos T, Aslam K, Shahbaz Anwar M, Imran M, Latif H. XRD and SEM analysis of a laser-irradiated cadmium. Laser Physics. 2007; **17**(9):1138-1145

[21] Umm-i-Kalsoom, Bashir S, Ali N, Akram M, Mahmood K, Ahmad R. Effect of ambient environment on excimer laser induced micro and nano-structuring of stainless steel. Applied Surface Science. 2012;**261**:101-109

[22] Ikhlaq U, Ahmad R, Saleem S, Shah MS, Kalsoom U, Khan N, Khalid N. Argon gas concentration effects on nanostructured molybdenum nitride layer growth using 100 Hz pulsed dc glow discharge. The European Physical Journal Applied Physics. 2012;**59**: 20801

[23] Noyan IC, Cohen JB. Residual Stress-Measurement by Diffraction and Interpretation. New York: Springer-Verlag; 1987

[24] Khan IA, Hassan M, Ahmad R, Qayyum A, Murtaza G, Zakaullah M, Rawat RS. Nitridation of zirconium using energetic ions from plasma focus device. Thin Solid Films. 2008;**516**(23):8255-8263

[25] Gurarie VN, Otsuka PH, Jamieson DN, Prawe S. Crack-arresting compression layers produced by ion implantation. Nuclear Instruments and Methods in Physics Research B. 2006;**242**(1-2):421-423

[26] Mahmood K, Farid N, Ghauri IM, Afzal N, Idrees Y, Mubarik FE. Effects of laser irradiation on the mechanical response of polycrystalline titanium. Physica Scripta. 2010;**82**:045606-045613

[27] Kim BK, Hamaguchi HO. Mode assignments of the Raman spectrum of monoclinic zirconia by isotopic exchange technique. Physica Status Solidi (b). 1997;**203**:557-563

[28] Tan D, Lin G, Liu Y, Teng Y, Zhuang Y, Zhu B, Zhao Q, Qiu J. Synthesis of nanocrystalline cubic zirconia using femtosecond laser ablation. Journal of Nanoparticle Research. 2011;**13**:1183-1190

[29] Li M, Feng Z, Xiong G, Ying P, Xin Q, Li C. Phase transformation in the surface region of zirconia detected by UV Raman spectroscopy. The Journal of Physical Chemistry B. 2001;**105**:8107-8111

[30] Bashir S, Vaheed H, Mahmood Khaliq. Nanosecond pulsed laser ablation of brass in a dry and liquid-confined environment. Applied Physics A. 2012

[31] Karimzadeh R, Zamir Anvari J, Mansour N. Nanosecond pulsed laser ablation of silicon in liquids. Applied Physics A: Materials Science and Processing. 2009;**94**:949-955

[32] Douglas BC, Graham KH. Pulsed Laser Deposition of Thin Films. Singapore, New York, chichester, Brisbane, Toronto: Wiley-interscience Publication; 1994

[33] Passchier CW, Trouw RAJ. Microtectonics. Berlin: Springer, Verlag; 1998

[34] Craciun V, Craciun D. Subsurface boiling during pulsed laser ablation of Ge. Physical Review B. 1998;**58**(11):6787-6790

[35] Borgstedt HU, editor. Liquid Metal Systems: Material Behavior and Physical Chemistry in Liquid. Springer Science and Business Media; 2012. p. 419

[36] Yang GW. Laser ablation in liquids: Applications in the synthesis of nanocrystals. Progress in Materials Science. 2007;**52**:648-698

[37] Amendola V, Meneghetti M. Laser ablation synthesis in solution and size manipulation of noble metal nanoparticles. Physical Chemistry Chemical Physics. 2009;**11**:3805-3821

[38] Lam J. Pulsed Laser Ablation in Liquid: Towards the Comprehension of the Growth Processes, in Physique. 2006, Universit'e Claude Bernard Lyon 1: Ecole Doctorale de Physique et d'Astrophysique de Lyon

[39] Warcholinski B, Gilewicz A. Journal of Achievements in Materials and Manufacturing Engineering. 2009;**37**:498

[40] Umm-i-Kalsoom S, Ahmad R, Ali N, Khan IA, Saleem S, Ikhlaq U, Khan N. Effect of power and nitrogen content on the deposition of CrN films by using pulsed DC magnetron sputtering plasma. Plasma Science and Technology. 2013;**15**(7):666-672

[41] Corengia P, Ybarra G, Moina C, Cabo A, Broitman E. Microstructural and topographical studies of DC-pulsed plasma nitrided AISI 4140 low-alloy steel. Surface and Coatings Technology. 2005;**200**:2391-2397